Particle Acceleration and Fractional Transport in Turbulent Reconnection

Heinz Isliker[1] , Theophilos Pisokas[1], Loukas Vlahos[1] , and Anastasios Anastasiadis[2]
[1] Department of Physics, Aristotle University of Thessaloniki, GR-52124 Thessaloniki, Greece
[2] Institute for Astronomy, Astrophysics, Space Applications and Remote Sensing, National Observatory of Athens, GR-15236 Penteli, Greece

Abstract

We consider a large-scale environment of turbulent reconnection that is fragmented into a number of randomly distributed unstable current sheets (UCSs), and we statistically analyze the acceleration of particles within this environment. We address two important cases of acceleration mechanisms when particles interact with the UCS: (a) electric field acceleration and (b) acceleration by reflection at contracting islands. Electrons and ions are accelerated very efficiently, attaining an energy distribution of power-law shape with an index 1–2, depending on the acceleration mechanism. The transport coefficients in energy space are estimated from test-particle simulation data, and we show that the classical Fokker–Planck (FP) equation fails to reproduce the simulation results when the transport coefficients are inserted into it and it is solved numerically. The cause for this failure is that the particles perform Levy flights in energy space, while the distributions of the energy increments exhibit power-law tails. We then use the fractional transport equation (FTE) derived by Isliker et al., whose parameters and the order of the fractional derivatives are inferred from the simulation data, and solving the FTE numerically, we show that the FTE successfully reproduces the kinetic energy distribution of the test particles. We discuss in detail the analysis of the simulation data and the criteria that allow one to judge the appropriateness of either an FTE or a classical FP equation as a transport model.

Key words: acceleration of particles – convection – diffusion – magnetic reconnection – plasmas – turbulence

1. Introduction

A few years ago, it was believed that the prominent acceleration mechanisms for space and astrophysical plasmas were (1) the large-scale DC electric field associated mostly with a reconnecting current sheet, (2) a spectrum of weak-amplitude MHD waves, and (3) the diffusive shock acceleration (see reviews by Melrose 1994; Miller et al. 1997). Which mechanism will dominate in the acceleration of charged particles in space, astrophysical, or laboratory plasmas was assumed to be related to the global energy release process(es) and the magnetic topology. The diffusion of particles in the six-dimensional position and momentum space is a complex problem in astrophysical and laboratory plasmas. In order to avoid this complexity, most studies concentrated their analysis on the energetics of the interaction of particles with isolated nonlinear MHD structures, e.g., reconnecting current sheets, a spectrum of small-amplitude MHD waves, and shocks.

The reconnecting current sheet was analyzed mostly as an isolated 2D or 3D structure for simplicity (Priest 2014). The processes related to the reconnection were assumed to be laminar, and the field lines smooth and well behaved. The conditions on the inflow and outflow sides of the reconnection zone have been taken, again for simplicity, to be quiescent. The structure was assumed to be "long" lived and "stable." The electric field associated with this highly idealized topology was approximated as $E \approx -V_A \times B/c + \eta j$, where V_A is usually close to the Alfvén speed, B is the ambient magnetic field, c is the speed of light, η is the resistivity, and j is the current density inside the reconnecting volume. The presence of broadband fluctuations of the magnetic and velocity fields, or the simultaneous presence of multiple reconnecting current sheets, or the generalization to a 3D magnetic topology, will change the above simplified picture and lead to a completely new scenario for magnetic reconnection, where current fragmentation will lead to strong turbulence ($\delta B/B \approx 1$). In a series of recent reviews, the road from a reconnecting current sheet(s) to the random formation of an ensemble of unstable current sheets (UCSs) inside a strongly turbulent plasma was outlined (e.g., Matthaeus & Velli 2011; Cargill et al. 2012; Hoshino & Lyubarsky 2012; Lazarian et al. 2012; Karimabadi & Lazarian 2013; Karimabadi et al. 2013, and references therein). This new environment of multiple UCSs was named turbulent reconnection. How electrons and ions will be accelerated by large-scale turbulently reconnecting plasmas in numerous space, astrophysical, or laboratory settings remains an open problem, and we will return to this issue in the next section.

The stochastic turbulent acceleration of charged particles by a spectrum of weak-amplitude MHD waves was initially analyzed by Kulsrud & Ferrari (1971) and Krymskii (1977), who closely followed the original idea of Fermi (1949). The proposed mechanism was based on the assumption that the magnetic field topology is simple and the excited MHD modes will be in resonance with the ions and/or electrons. The cause of excitation of the MHD waves was only schematically connected to the energy release process(es), and the fact that the waves were saturated at small amplitudes ($\delta B/B \ll 1$) was never justified. The main assumptions on which the stochastic wave–particle interaction was based are (a) the level of the excited waves should remain low for the quasilinear assumption to be valid and (b) the Fokker–Planck (FP) equation will also be valid (Achterberg 1981; Miller et al. 1990; Petrosian 2012). A break in these assumptions leads to a very different scenario for turbulence and particle acceleration (Biskamp & Welter 1989; Galsgaard & Nordlund 1996; Arzner & Vlahos 2004; Dmitruk et al. 2004; Turkmani et al. 2005; Arzner et al. 2006). Therefore, a second road from strong turbulence to turbulent reconnection was established in several 2D or 3D simulations over the last 30 years (see the review of Matthaeus & Velli 2011 and the cited literature).

Over the last 50 years, the analysis of turbulent shock followed the same simplifications outlined above for the reconnecting current sheet and the weak MHD waves. The analysis of the shock and acceleration of particles was always done in idealized topologies. The main scenario was based on a 2D smooth magnetic discontinuity (shock front) that moves with velocity V larger than the Alfvén speed inside a spectrum of MHD waves, which are convected with the flows upstream and downstream of the magnetic discontinuity. The charged particles are trapped and bounce from upstream to downstream of the shock front several times until they will escape from the vicinity of the shock. In the idealized case, two mechanisms can accelerate particles at the shock: the shock drift acceleration, which dominates in quasi-perpendicular shocks, and the diffusive shock acceleration, which dominates in quasi-parallel shocks (Drury 1983; Decker 1988; Kirk & Dendy 2001; Lee et al. 2012; Schure et al. 2012). The presented picture changes dramatically when the turbulence upstream and downstream in a 3D magnetic structure reaches very large amplitudes ($\delta B/B \approx 1$; see Caprioli & Spitkovsky 2014a, 2014b, 2014c) and drives turbulently reconnecting plasmas upstream and downstream of the shock front (Lazarian & Opher 2009; Drake et al. 2010; Karimabadi et al. 2014; Matsumoto et al. 2015; Zank et al. 2015; Burgess et al. 2016). How the new system of a shock with turbulently reconnecting plasmas upstream and downstream will evolve and how the turbulent flows may eventually transform the turbulent shock into a new environment full of randomly moving small-scale internal shock waves and UCSs (Achterberg 1990; Anastasiadis & Vlahos 1991, 1994; Schneider 1993) remain open problems. In other words, shock waves seem to follow the same pattern as the UCS(s) and strong MHD turbulence; asymptotically, they end up in a turbulent reconnection environment (e.g., Karimabadi et al. 2014 and cited references).

In summary, all three prominent acceleration mechanisms listed above, (a) magnetic reconnection, (b) strong MHD turbulence ($\delta B/B \approx 1$), and (c) shock waves, will evolve toward a new accelerator that has received considerable attention the last 10 years called turbulent reconnection.

In this article, we analyze the evolution of the energy distribution function of electrons and ions, their escape time, the role of collisions, and the transport properties of the particles inside a turbulent reconnection environment, where an ensemble of localized and highly effective accelerators is present. Our simulation box is large, and we follow the system for long times that are close to the observational ones, contrary to current Particle In Cell (PIC) simulations. The local accelerators that we consider may be UCSs, magnetic islands, or internal shocks, and they will systematically accelerate particles as they cross the turbulently reconnecting volume. The interaction of the charged particles with the small-scale UCS or internal shocks follows the scenario proposed by Fermi (1949, 1954), with the magnetic clouds being replaced by the more general concept of active scatterers. The particular aim of this study also is to explore the possible limitations of the FP approach in modeling transport and to show the importance of fractional transport equations (FTEs) in the context of turbulent reconnection.

In Section 2, we analyze the local dynamics of particles in their interaction with typical scatterers (i.e., UCSs). In Section 3, we introduce a fractional approach for modeling transport, in comparison with the classical, FP approach and the classical transport coefficients. In Section 4, we construct a 3D lattice gas model, where a small number of grid sites are active (scatterers), and we study the energy evolution of an initial distribution of particles injected into this environment. In Section 5, we examine the transport properties of particles inside a collection of UCSs, using both the fractional and the FP approaches. In the final section, we discuss the implications of our results for explosive phenomena in the solar corona and list our main conclusions.

2. Particle Acceleration by an Ensemble of Unstable Current Sheets

Matthaeus et al. (1984) and Ambrosiano et al. (1988) were the first to analyze numerically the test-particle dynamics inside a 2D turbulently reconnecting environment, using the electromagnetic fields from the simulations of Matthaeus & Montgomery (1980) and Matthaeus & Lamkin (1986). These original studies analyzed the role of turbulent reconnection in the acceleration of test particles. Several studies returned to this problem many years later to analyze the interaction of particles in 3D topologies, where the turbulently reconnecting environment was generated by large-amplitude waves or multiple UCSs, using the MHD equations as the main tool for understanding the current fragmentation and formation of turbulently reconnecting environments (Dmitruk et al. 2003, 2004; Arzner & Vlahos 2004; Turkmani et al. 2005; Arzner et al. 2006; Onofri et al. 2006; Kowal et al. 2011; Gordovskyy & Browning 2011). The resistive MHD equations can handle the large scales in space, astrophysical, and laboratory systems, and they can follow the formation of UCSs, but they completely miss the kinetic evolution. The statistical properties of UCSs inside a 2D or 3D turbulently reconnecting environment have also been analyzed by Uritsky et al. (2010), Servidio et al. (2011), and Zhdankin et al. (2013).

On different scales, the analysis of the UCS(s) through the use of PIC codes focuses on the details of the dynamics of the particles. They follow the formation of plasmoids and their interaction with electrons and ions (Drake et al. 2006; Onofri et al. 2006; Guo et al. 2014, 2015; Dahlin et al. 2015; Hoshino 2012). The PIC simulations, both in 2D or 3D, use periodic boundary conditions; the dimensions of the simulation box are extremely small (several meters for solar coronal parameters), and the timescale of their evolution is a few thousands of ω_e^{-1}, where ω_e is the electron plasma frequency (for the solar corona, this is several microseconds). Thus, the PIC simulations follow the kinetic aspects of turbulent reconnection in a very small periodic volume and for very short times.

It is important to separate the particle dynamics inside an evolving UCS from the evolution in the global environment where particles travel between UCSs, which serve as scatterers, in analogy with the magnetic clouds envisioned by Fermi (1949). Particles travel a distance λ_{sc} before they interact with a UCS, and the energy gain as they "cross" the scatterer is dW. The energy increment (dW) can be either stochastic (see Pisokas et al. 2017), when the particles interact with magnetic fluctuations, or systematic ($dW > 0$), when they interact with UCSs. Based on current PIC simulations, the energy increments, when the particles escape from the locally evolving UCS, are always positive (see Dahlin et al. 2015; Guo et al. 2015; Matsumoto et al. 2015).

Vlahos et al. (2004, 2016) and Pisokas et al. (2017) attempted to combine the large-scale dynamics of particles

with their dynamics at the UCS, assuming a very simple interaction of the particles with the locally evolving UCS (see also the recent reviews by Cargill et al. 2012; Lazarian et al. 2012; Karimabadi et al. 2013, 2013). It was assumed that the spatial and temporal scales of the UCSs are so small compared with the system under study that they can be approximated with nodes inside the large-scale simulation box, and that their interaction with the particles is instantaneous.

2.1. Systematic Acceleration by Random Electric Fields

The particle dynamics inside UCSs is complex, since internally UCSs are also fragmented and the particles that interact with the fragments of a UCS can lose and gain energy on the microscopic level of description. However, on average and over the entire simulation domain, particles gain energy systematically before exiting the UCS; see Figure 6(c) of Guo et al. (2015) or Figure 3(d) in Matsumoto et al. (2015) and the related discussion. We approximate the macroscopic energy gain as

$$\Delta W = |q| E_{\mathrm{eff}}\, \ell_{\mathrm{eff}}, \qquad (1)$$

where $E_{\mathrm{eff}} \approx (V/c)\, \delta B$ is the measure of the effective electric field of the UCS and δB is the fluctuating magnetic field encountered by the particle, which is of stochastic nature, related to the stochastic fluctuations induced by reconnection. ℓ_{eff} is the characteristic length of the interaction of the particle with the UCS and should be proportional to E_{eff}, since a small E_{eff} will be related to small-scale UCS. In other words, the UCS is a complex structure that always accelerates the charged particle crossing it. The scenario in the method used here is as follows: particles approach the scatterers with an initial kinetic energy W_0 and depart with an energy $W = W_0 + \Delta W$, where the energy gain ΔW on the macroscopic level is systematic and follows the statistical properties of the fluctuations δB.

2.2. Systematic Fermi Acceleration at Contracting Islands

The systematic and macroscopic energy gain from the acceleration by reflection at contracting islands in a UCS can be written as a variant of the classical Fermi acceleration for relativistic particles when only head-on collisions are taken into account and the energy increase is always positive,

$$\Delta W = \Gamma \left[\left(\frac{V_A}{c} \right)^2 + \left(\frac{2 V_A u_\parallel}{c^2} \right) \right] W \qquad (2)$$

(Longair 2011), where $u_\parallel$ is the component of the velocity of the particle parallel to the magnetic field and Γ is the Lorenz factor. For nonrelativistic particles, we have

$$\Delta W = W \left(\frac{V_A}{c} \right) \left(\frac{u_\parallel}{c} \right) = W \left(\frac{V_A}{c} \right) \left(\frac{u}{c} \right) \cos \phi, \qquad (3)$$

where ϕ is a random angle, $-\pi/2 < \phi < \pi/2$. (de Gouveia dal Pino & Lazarian 2005; Drake et al. 2006; Hoshino 2012; Dahlin et al. 2015; Guo et al. 2015).

The important difference between the systematic electric field "scatterer" and the systematic Fermi acceleration is the fact that dW is not a function of W in the first case, in contrast to the second case.

3. Classical and Fractional Approach to Modeling Transport

3.1. Classical Transport Coefficients and the FP Equation

The energy convection coefficient, which reflects the systematic aspects of acceleration, is given as

$$F(W, t) = \frac{\langle W(t + \Delta t) - W(t) \rangle_W}{\Delta t}, \qquad (4)$$

and the energy diffusion coefficient, which describes the statistic nature of acceleration, is defined as

$$D(W, t) = \frac{\langle (W(t + \Delta t) - W(t))^2 \rangle_W}{2 \Delta t}, \qquad (5)$$

where $\langle \ldots \rangle_W$ denotes the conditional average that $W(t) = W$, which accounts for the functional dependence of the transport coefficients on the energy W (see, e.g., Ragwitz & Kantz 2001). In the current literature, these coefficients were often estimated analytically by using several simplifying assumptions (Drake et al. 2013; Guo et al. 2014; Zank et al. 2015), whereas we here determine them directly from the particle dynamics, as in Vlahos et al. (2016). For the numerical estimate of the coefficients, the energies of the particles at time t are divided into logarithmically equispaced bins, and the coefficients are estimated for each bin separately (i.e., we apply binned statistics). Δt is a small time interval, just large enough so that most particles exhibit discernible changes in their kinetic energy (the theoretical limit $\Delta t \to 0$ can of course practically not be applied).

As as simplification, we here ignore spatial diffusion and consider that the particles diffuse only in energy space. The well-established assumption in space and astrophysical plasmas is that the interaction of particles with UCSs is such that the FP equation will be valid,

$$\frac{\partial n}{\partial t} + \frac{\partial}{\partial W} \left[Fn - \frac{\partial (Dn)}{\partial W} \right] = -\frac{n}{t_{\mathrm{esc}}} + Q, \qquad (6)$$

where n is the energy distribution function, t_{esc} is the escape time from an acceleration volume with characteristic size L, Q is the injection rate, and F and D are the transport coefficients defined above. The validity of the FP equation is based on the hypothesis that the particles execute a kind of Brownian motion in energy space as they interact with the localized UCSs, with the random walk steps being small in the sense that they have finite mean and variance (see the remarks below). In Section 5, we use data from the test particle approach to assess the validity of the FP equation in a turbulently reconnecting plasma.

Using the pseudo-spectral method with rational Chebyshev polynomials as the base functions in energy space, we numerically integrate the FP equation on the semi-infinite energy interval $[0, \infty)$, with the time stepping being implemented in the form of the implicit backward Euler method (see, e.g., Boyd 2001).

3.2. Fractional Transport Equation

FTEs allow non-local and anomalous transport phenomena to be described. To derive the FTE, we here follow Isliker et al.

(2017). A variant of the Chapman–Kolmogorov equation,

$$n(W, t) = \int dw \int_0^t d\tau\, n(W - w, t - \tau)\, q_w(w) q_\tau(\tau)$$
$$+ n(W, 0) \int_t^\infty q_\tau(\tau) d\tau, \qquad (7)$$

allows for a general description of transport in energy space; see, e.g., Klafter et al. (1987) and Klages et al. (2008). The conservation law in Equation (7) can be interpreted as a Continuous Time Random Walk process (a generalization of the classical Brownian motion). The random walk steps in energy w are distributed according to the probability density q_w, and the time intervals τ for these steps to be performed obey the probability density function q_τ (the two probability densities are assumed to be independent in order to simplify the approach). When both distributions of increments, q_w and q_τ, have finite mean and variance (as, e.g., in the case where they are Gaussian distributions), then, through a standard procedure using Taylor expansions, the FP equation (Equation (6)) can be derived from Equation (7); see,e.g., Gardiner (2009). In the following, we do not make the assumption that the increments are small and explicitly allow for infinite mean or variance.

In order to derive a mesoscopic equation, we make a Fourier Laplace transform ($W \to k$, $t \to s$) of Equation (7) and make use of the respective convolution theorems, which yields the Montroll–Weiss equation (written in slightly nonstandard form),

$$\tilde{\hat{n}}(k, s) = \tilde{\hat{n}}(k, s)\, \hat{q}_w(k) \tilde{q}_\tau(s) + \hat{n}(k, 0) \frac{1 - \tilde{q}_\tau(s)}{s} \qquad (8)$$

(Montroll & Weiss 1965; Klafter et al. 1987).

For the distributions of increments, we employ the stable Levy distributions, which are defined in Fourier (k) or Laplace (s) space through their so-called characteristic functions. For the distribution of energy increments, we assume symmetric stable Levy distributions $\hat{q}_w(k) = \exp(-a|k|^\alpha)$, with $0 < \alpha \leqslant 2$, which have a power-law tail in energy space, $q_w(w) \sim 1/w^{1+\alpha}$ for $\alpha < 2$ and w large, and for $\alpha = 2$ they are Gaussian distributions (Hughes 1995). For the waiting time distribution, we consider one-sided stable Levy distributions (expressed in Laplace space), $\tilde{q}_\tau = \exp(-bs^\beta)$ with $b > 0$ and $0 < \beta \leqslant 1$, which exhibit a power-law tail, $q_\tau \sim 1/\tau^{1+\beta}$ for $\beta < 1$ and τ large, and for $\beta = 1$ they are Dirac delta functions, $q_\tau(\tau) = \delta(\tau - b)$ (Hughes 1995).

The last step in the derivation of the FTE consists in applying the fluid limit, i.e., we assume that w and τ are large, and thus, in turn, that k and s are small (e.g., Klages et al. 2008 and references therein), which allows approximating the distributions of increments by a Taylor expansion up to first order, $\hat{q}_w \approx 1 - a|k|^\alpha$ and $\tilde{q}_\tau \approx 1 - bs^\beta$. Inserting the approximations into Equation (8) yields

$$\tilde{\hat{n}}(k, s) = \tilde{\hat{n}}(k, s)\, (1 - a|k|^\alpha - bs^\beta) + \hat{n}(k, 0) bs^{\beta-1}, \quad (9)$$

or, by rearranging,

$$bs^\beta \tilde{\hat{n}}(k, s) - bs^{\beta-1} \hat{n}(k, 0) = -a|k|^\alpha \tilde{\hat{n}}(k, s). \qquad (10)$$

The latter equation actually contains fractional derivatives and can be written as an FTE,

$$b D_t^\beta n = a D_{|W|}^\alpha n, \qquad (11)$$

where D_t^β is the Caputo fractional derivative of order β, defined in Laplace space as

$$\mathcal{L}(D_t^\beta n) = s^\beta \tilde{n}(W, s) - s^{\beta-1} n(W, 0), \qquad (12)$$

and $D_{|W|}^\alpha$ is the symmetric Riesz fractional derivative of order α, defined in Fourier space as

$$\mathcal{F}(D_{|W|}^\alpha n) = -|k|^\alpha \hat{n}(k, t); \qquad (13)$$

see, e.g., Klages et al. (2008) and Bian & Browning (2008). Note that for $\beta = 1$ and $\alpha = 2$ or 1, Equation (11) includes the cases of a pure diffusion or convection equation, respectively, corresponding to the classical FP equation.

The derivation of the FTE makes it clear that the indices of the power-law tails, if any, of the distributions of increments $q_w(w)$ and $q_\tau(\tau)$ determine the order of the fractional derivatives. On the other hand, if there are no power-law tails and both the mean and variance of the distributions of increments are finite, then the respective derivatives are classical and of integer order. Finally, if both the time and energy derivatives are of integer order, then the classical FP equation is appropriate.

The parameters of the FTE are α, a and β, b, which need to be estimated from the test-particle data. As pointed out above, α is given by the index z of the power-law tail of $p_w(w)$ as $\alpha = -z - 1$. The characteristic function approach (Koutrouvelis 1980; Borak et al. 2005) is a second method to determine α and also a. Based on the sample of increments $\{w_j\}$ from the test-particle simulations, the estimator $\tilde{q}_w$ of the characteristic function $\hat{q}_w$ is defined as

$$\tilde{q}_w(k) = \langle e^{ikw_j} \rangle_j \qquad (14)$$

for a suitable set of k-values. If the w_j are distributed according to a stable Levy distribution, then $\hat{q}_w(k) = \exp(-a|k|^\alpha)$ should hold, and α will equal the slope of a linear fit to $\ln(-\ln|\tilde{q}_w|^2)$ as a function of $\ln k$, and the intercept with the y-axis will yield $\ln(2a)$.

Before turning to the temporal part of the FTE and its parameters β and b, we need to specify how we define the energy increments w_j^n (with j the particle index and n the index that labels temporally subsequent increments). In the lattice model introduced below, the energizations are discrete events that take place in the instantaneous interactions of the particles with the scatterers. So, one choice could be to let w_j^n denote these instantaneous changes of particle energy. This choice though has practical difficulties in its application, e.g., to test-particle simulations, as, e.g., in Isliker et al. (2017), where the energizations may or may not be localized, and where there would be very likely some arbitrariness in the definition of the waiting times. A second choice, which, as in Isliker et al. (2017), we adopt here, is to monitor the particles at fixed time intervals of duration Δt and to consider the increments to be defined as the energy change over the time interval Δt, so that the increments w_j^n become equal to the energy differences $[W(t + \Delta t) - W(t)]_j$ in the definitions of F and D, Equations (4) and (5),

$$w_j^n \equiv w_j(t) := [W(t + \Delta t) - W(t)]_j. \qquad (15)$$

The definition of the increments w_j^n used here then implies that the waiting times are constant (Δt), and thus the waiting time distribution is of the form $p_\tau(\tau) = \delta(t - \Delta t)$, from which it follows, as explained above, that $\beta = 1$ and $b = \Delta t$. Thus, in

the following, we consider the FTE to be of the form

$$\partial_t n = (a/\Delta t) D_{|W|}^\alpha n - n/t_{esc}, \qquad (16)$$

with an ordinary, first-order derivative in the time direction and a fractional derivative in the energy direction, and where we also have added the escape term $-n/t_{esc}$.

We solve the FTE numerically by using the Grünwald–Letnikov definition of fractional derivatives (e.g., Kilbas et al. 2006), implemented in the matrix form of Podlubny et al. (2009), and in particular we use the derivative scheme of Podlubny et al. (2013) for non-equidistant grid points, which allows the same grid points in $[0, \infty)$ to be used as for the solution of the FP equation above. In the time direction, the implicit backward Euler scheme is used. Since the FTE has been derived here as a tool for modeling long tails at the high-energy side of the energy distribution, which is the main interest of this study, we only apply the fractional derivative above energies of 10 eV in numerical applications (note, e.g., that the fluid limit has been applied in the derivation of the FTE).

4. Particle Dynamics in Turbulently Reconnecting Plasma: Numerical Study

4.1. Initial Setup

We use a lattice gas model for the simulation of turbulent reconnection, in the form of a 3D grid ($N \times N \times N$) with grid size $\ell = L/(N - 1)$ and linear extent L. A randomly chosen, small fraction $R = N_{sc}/N^3$ (5%–20%) of grid sites is marked as active scatterers; the rest of the grid sites are inactive. The mean free path of the particles between scatterers can be determined as $\lambda_{sc} = \ell/R$, and the density of the scatterers follows $n_{sc} = R \times N^3/L^3$.

At time $t = 0$, a large number of particles (electrons or ions) are distributed in the simulation box over randomly chosen grid sites. The particles initially follow a velocity distribution $n(W, t = 0)$ of Maxwellian shape with temperature T, and they move into random directions on the grid (the particles are bound to follow the grid lines).

In encounters with active grid sites, the particles' kinetic energy changes by the amount ΔW (the amount depends on the kind of scatterers considered, and in any case, we here address only the case of systematic acceleration, where ΔW is always positive; see Section 2). After the interaction with a scatterer, a particle again moves in a random direction, until the next encounter with a scatterer, or until it reaches one of the grid boundaries. The smallest possible free travel distance between scattering events is given by the grid size (ℓ). The scattering events are considered to be instantaneous, so the timing is determined by the free travel times $\Delta t = s/v$, where v is the particle's velocity and s is the distance it travels in between subsequent scatterings.

4.2. Systematic Acceleration by Random Electric Fields

4.2.1. Open Boundary Conditions

A 2D version of this model was presented by Vlahos et al. (2016), which we extend here to a 3D acceleration volume. Following Equation (1), each scattering at an active grid point increases the particle's energy by $\Delta W = |q| \left(\frac{V_A}{c} \delta B\right) \ell_{\text{eff}}$.

The parameters used in this article are related to the plasma parameters in the low solar corona. We choose the strength of the magnetic field to be $B = 100$ G, the density of the plasma to be $n_0 = 10^9$ cm^{-3}, the ambient temperature to be around 10 eV, and the length L of the simulation box to be 10^9 cm. The Alfvén speed is $V_A \approx 7 \cdot 10^8$ cm s^{-1}, so V_A is comparable with the thermal speed of the electrons. We assume that δB takes random values following a power-law distribution with index 5/3 (Kolmogorov spectrum), and $\delta B \in [10^{-5}$ G, 100 G]. The effective electric field $E_{\text{eff}} = (V_A/c)\delta B$ lies approximately in $E_{\text{eff}} \in [2 \cdot 10^{-7}, 2]$ statV/cm. We also assume the effective length ℓ_{eff} to be a linear function of E_{eff}, $\ell_{\text{eff}} = aE_{\text{eff}} + b$, where the constants a and b are determined by restricting the size of ℓ_{eff} to the range from 10 m to 1 km (see also Zhdankin et al. 2013 for the statistical properties of UCS). Applying these values to Equation (1), we find that the energy change ΔW varies between 10^{-13} eV and 10^8 eV (due to the power-law distribution of δB, small energy changes are much more frequent).

We consider the grid to be open, so particles can escape from the acceleration region when they reach any boundary of the grid. We assume in this setup that only $R = 10\%$ of the $N^3 = 601^3$ grid sites are active. The mean free path is thus given as $\lambda_{sc} = \ell/R \approx 1.7 \cdot 10^7$ cm, which coincides with the value estimated numerically by tracing particles inside the simulation box.

As Figure 1(a) shows, the particles execute a classical random walk on the grid in position space; though/yet in energy space, the dynamics is of the form of a systematic random walk—see Figure 1(b)—there are exclusively positive energy increments dW (for details of the energy gain within the UCS, see Dahlin et al. 2015; Guo et al. 2015; Matsumoto et al. 2015; Isliker et al. 2017).

We monitor the electron population, injected at $t = 0$, until half of it have escaped, which happens at $t_{1/2} = 4.5$ s. The electrons that remain inside the box at $t = 1$ s are distributed as shown in Figure 2(a). The energization process heats the low-energy particles below 1 keV, where the distribution follows a Maxwellian with temperature 40 eV. The high-energy part of the distribution exhibits a clear power-law tail, with index $k \approx 1.7$, which extends from about 1 keV to 100 MeV. The power-law tail is formed in a few milliseconds, and it persists even when more electrons escape from the acceleration volume. This implies that the acceleration process is extremely fast.

Using a higher initial temperature of 100 eV for the particles basically does not affect the high-energy part of the final energy distribution; as Figure 2(b) shows, the extent and the index of the power-law tail remain almost unchanged, and only at the low-energy part are the particles heated to a higher temperature of 250 eV.

Each of the escaping electrons leaves with a different energy and at a different time, depending on its initial energy and the energization resulting from the scattering events. We term the time a particle reaches any boundary of the acceleration volume its escape time, t_{esc}, and the energy it carries at that moment its escape energy. The distribution of the escape energy, presented in Figure 3(b), exhibits a shape very similar to that of the particles that remain inside (Figure 2(a)); a power-law tail is formed with index 1.4 at energies above 1 keV. Figure 3(a) shows the distribution of the escape times for all of the escaping electrons; it is uniform up to about 10 s, and then it turns into a power-law tail with index ≈ 2, up to the time of 10^4 s. The median value of the escape times of all electrons can
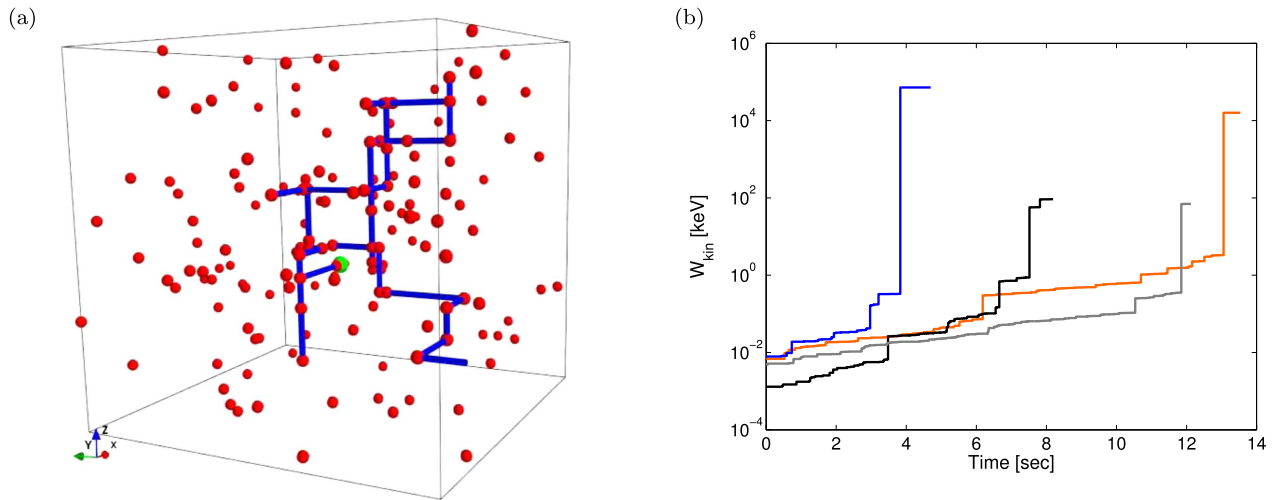
(a)

(b)

Figure 1. (a) Typical trajectory in the 3D simulation box (blue). The red spheres mark the randomly distributed UCSs (active grid sites). (b) Energy as a function of time for a few selected particles.

be used as an estimate for the characteristic escape time from the system, $t_{esc} \approx 4.5$ s, which coincides with its half-time $t_{1/2}$ defined above. Using binned statistics, the escape time can be interpreted to be a function of the escape energy, as shown in Figure 3(c). We observe two distinct regions, the high-energy one, extending from 1 keV to 1 MeV, and the low-energy one, below 1 keV. At low energies, there is a power-law functional form, $t_{esc} \propto W_{esc}^{0.4}$. At higher energies, the function becomes constant, assuming the value $t_{esc} \approx 5$. This indicates that the high-energy particles, which form the power-law tail of the energy distribution, stay the longest in the acceleration volume, and with that, they basically determine the mean escape time. Also, the degree of energization is thus directly correlated with the time that the particles stay inside the system only for low-energy particles—the high-energy particles presuppose the longest, yet constant and independent of the particles' energy, time to be accelerated in the system. The number of scatterings as a function of the final energy (again estimated using binned statistics) yields a very similar picture—see Figure 3(d)—only for the low-energy particles does the final energy increase with the increasing number of scatterings; the high-energy particles all undergo approximately the same number of 1000 scatterings, independent of their final energy.

There are two key parameters for the turbulent reconnection analyzed here. The first is the mean free path in between encounters with the scatterers, λ_{sc}, which is controlled by the density of the latter, n_{sc}, as defined in Section 4.1. Changing any of the parameters while keeping the scatterer density fixed has no effect on the results. Thus, for simplicity, we fix both the size of the acceleration volume and the number of grid points to constant values, so that the density of the scatterers depends solely on the active-point ratio R. As this ratio varies in the range $0.05 \leqslant R \leqslant 0.2$ (i.e., 10^7 cm $\leqslant \lambda_{sc} \leqslant 10^8$ cm), the acceleration time remains extremely small, while the escape time varies from 5.5 to 1.7 s with an almost linear decrease. The energy distribution, on the other hand, maintains its power-law form. The second important free parameter of the system is the index $z_{\delta B}$ of the power-law distribution of the fluctuations of the magnetic field, δB. As it varies from $1 \lesssim z_{\delta B} \lesssim 3$, the power-law index k of the particles' energy distribution follows approximately the evolution of $z_{\delta B}$.
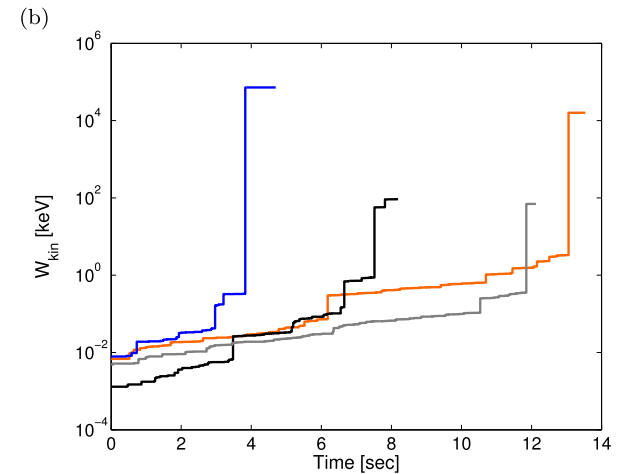
The results discussed so far refer to electrons. Using ions in the simulations, we find that the evolution of the energy distribution exhibits the same features as that of the electrons, except for the timescales involved. The ion population half-time amounts to 195 s, as does the median escape time (the escape times now vary from 0.1 to 10^6 s), while the acceleration time is approximately 250 s. Keeping in mind these different timescales, the escape characteristics are also similar (see Figure 3): the escape energy and escape time distributions have a power-law tail with indices 1.5 and 2.1, respectively, and t_{esc} and the number of scatterings per particle as functions of W_{esc} retain a power-law shape at low energies and turn over to become constant at large energies. In other words, ions follow very closely the characteristics of the electrons, yet with a remarkable delay of several minutes (for the parameters used here).

In order to investigate the role of collisions, we apply a modified version of the collision model of Lenard & Bernstein (1958), where the charged particles undergo Coulomb collisions with a background plasma population of temperature T (which we choose to be equal to the particles' initial temperature). As described in Pisokas et al. (2017), if a particle with initial velocity $v(t)$ travels the distance s between two subsequent encounters with scatterers during a time interval τ, then the final velocity $v(t + \tau)$ can be computed with an analytical expression (Gillespie 1996),

$$v(t + \tau) = v(t)\mu + \sigma_v N_1, \qquad (17)$$

where $\mu = e^{-\nu_v \tau}$, $\sigma_v^2 = \frac{k_B T}{m}(1 - \mu^2)$, and N_1 is a Gaussian random variable with mean 0 and standard deviation 1. We note that in this modified model the collision frequency ν_v is velocity dependent, $\nu_v \propto 1/v(t)^3$, as appropriate for a fully ionized plasma, and that v here is the nonrelativistic speed that is bounded by the speed of light.

In Figure 4, we compare the energy distribution of the electrons remaining inside the acceleration volume for the cases with and without collisions at $t = t_{acc} = 3.5$ s. The collisional mean free path is 180 times smaller than the mean free path between scatterings ($\lambda_{coll} = 9.27 \cdot 10^4$ cm), so collisions are relevant, yet they affect only the low-energy part of the distribution, below 100 eV; the high-energy part shows a
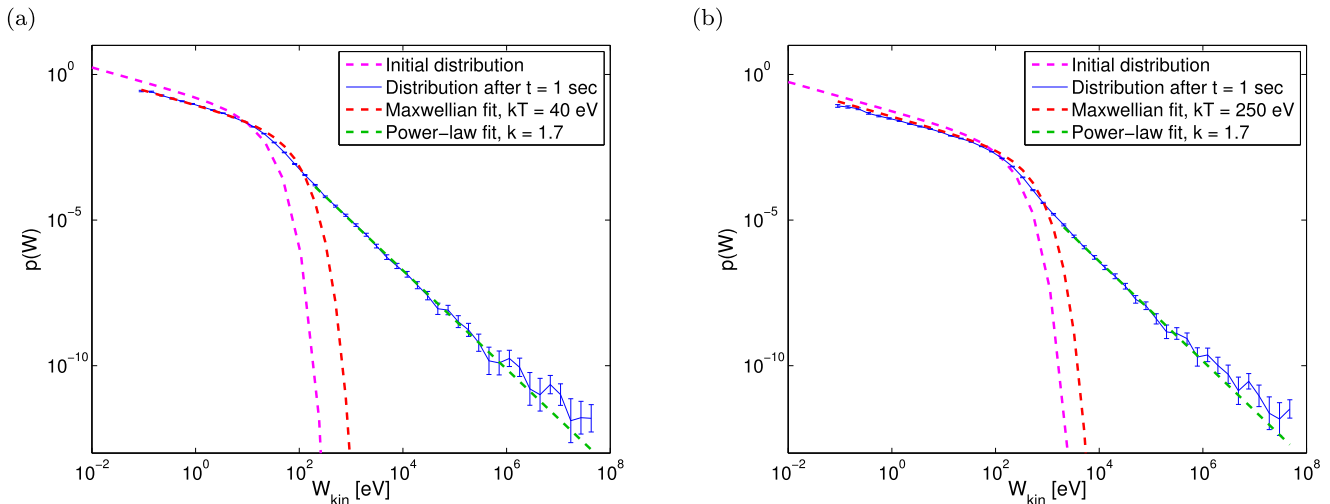
(a)

(b)

Figure 2. Energy distribution at $t = 0$ and $t = 1$ s of the electrons that have remained inside the box, for an initial temperature of (a) 10 eV and (b) 100 eV.

power-law shape with the same index as in the collisionless case, $k = 1.7$

4.2.2. Periodic Boundary Conditions

We now impose periodic boundary conditions, i.e., any particle that reaches a boundary grid site continues its motion from the corresponding grid site on the opposite boundary, without any other changes in the setup.

The evolution of the energy distribution of electrons is shown in Figure 5, together with the temporal evolution of the power-law exponent of its tail. The energy distribution develops a power law in a few milliseconds, with an index that ultimately drops to an asymptotic value of $k = 1$ at $t \approx 16$ s. After that time, the distribution just extends to higher energies, without changing its power-law shape any longer. We note that this result agrees very well with numerous 3D PIC simulations (see, e.g., Guo et al. 2015; Matsumoto et al. 2015).

Again, the crucial parameter for the evolution of the system is the mean free path between scatterings λ_{sc}. An increase of the ratio of active grid sites R from 0.05 to 0.2 leads to a decrease in the time for the power-law-shaped energy distribution to reach a specific index, namely, from 28 s to 7 s for $k = 1.1$, and from 33 s to 7 s for $k = 1$.

As for $z_{\delta B}$, we observe that

for indices $z_{\delta B}$ below 2, the asymptotic energy distribution exhibits a power law with $k = 1$, and for $2 \lesssim z_{\delta B} \lesssim 3$, the index of the asymptotic power law is $k \geqslant z_{\delta B}$.

4.3. Systematic Fermi Acceleration at Contracting Islands

We now consider systematic Fermi acceleration, with the energy gain during a particle–scatterer interaction given by Equation (2), and otherwise maintaining the setup as described in the first part of the current section. Using the parameters presented in Section 4.2, we find that the energization is much more effective, with a typical energy gain of $\approx$600 eV per scattering event. We thus repeat the analysis in a larger acceleration volume with characteristic length $L = 5 \times 10^9$ cm, with open boundaries, and with only 5% of the grid points being active, which leads to a larger mean free path among the scatterers, $\lambda_{sc} = 1.67 \times 10^8$ cm. With these changes, the energy distribution of the electrons exhibits a narrow power-law distribution with index $k \approx 3.5$ at 100 ms, which, with increasing time, gains in

extent and the power-law index decreases, until it stabilizes at the value of $k = 1$ at 1 s; for larger times, the power law still widens, yet the index no longer changes.

We present two time instances of the evolution of the energy distribution in Figure 6(a). The first one is the energy distribution at $t = 0.7$ s, where the power-law index has attained the value $k = 1.1$. At this time, close to the asymptotic state, almost 90% of the particles are still inside the system; the high intensity of the energization process leads the system to its asymptotic state before a considerable percentage of the initial population escapes. The application of periodic boundary conditions results therefore in similar power-law distributions, and it has only minor effects on the characteristics of the system before its stabilization. The other time instance of interest is the half-time of the system, when 50% of the particles have escaped from the acceleration box, which once again coincides with the escape time, defined as the median of the individual escape times of the particles, $t_{1/2} \approx t_{esc} \approx 2.3$ s. The power-law-shaped energy distribution still exhibits the index $k = 1$, which persists for longer times, even when the vast majority of the particles have escaped. We can clearly conclude that the power-law shape and its index are characteristic for the energization process and they are independent of the boundary conditions.

By solving Equation (2), one would expect an exponential growth of the mean energy (see Pisokas et al. 2017). The mean energy of the electrons as a function of time in Figure 6(b) clearly agrees with this prediction, from which we can estimate the acceleration time for the system as the growth rate, $t_{acc} = 0.22$ s.

Also, for systematic Fermi acceleration at contracting islands, the key parameter for the system remains the mean free path of the particles, λ_{sc}, and it actually is reciprocally related to the acceleration and stabilization times, yet it has no significant effect on the escape time, which can be attributed to the high intensity of the energization process.

5. Transport Properties of Particles Inside a Turbulently Reconnecting Plasma

For one case of electric field acceleration and one case of acceleration at contracting islands, we now determine the transport coefficients $F(W)$, Equation (4), and $D(W)$, Equation (5), as a function of energy. We then insert the
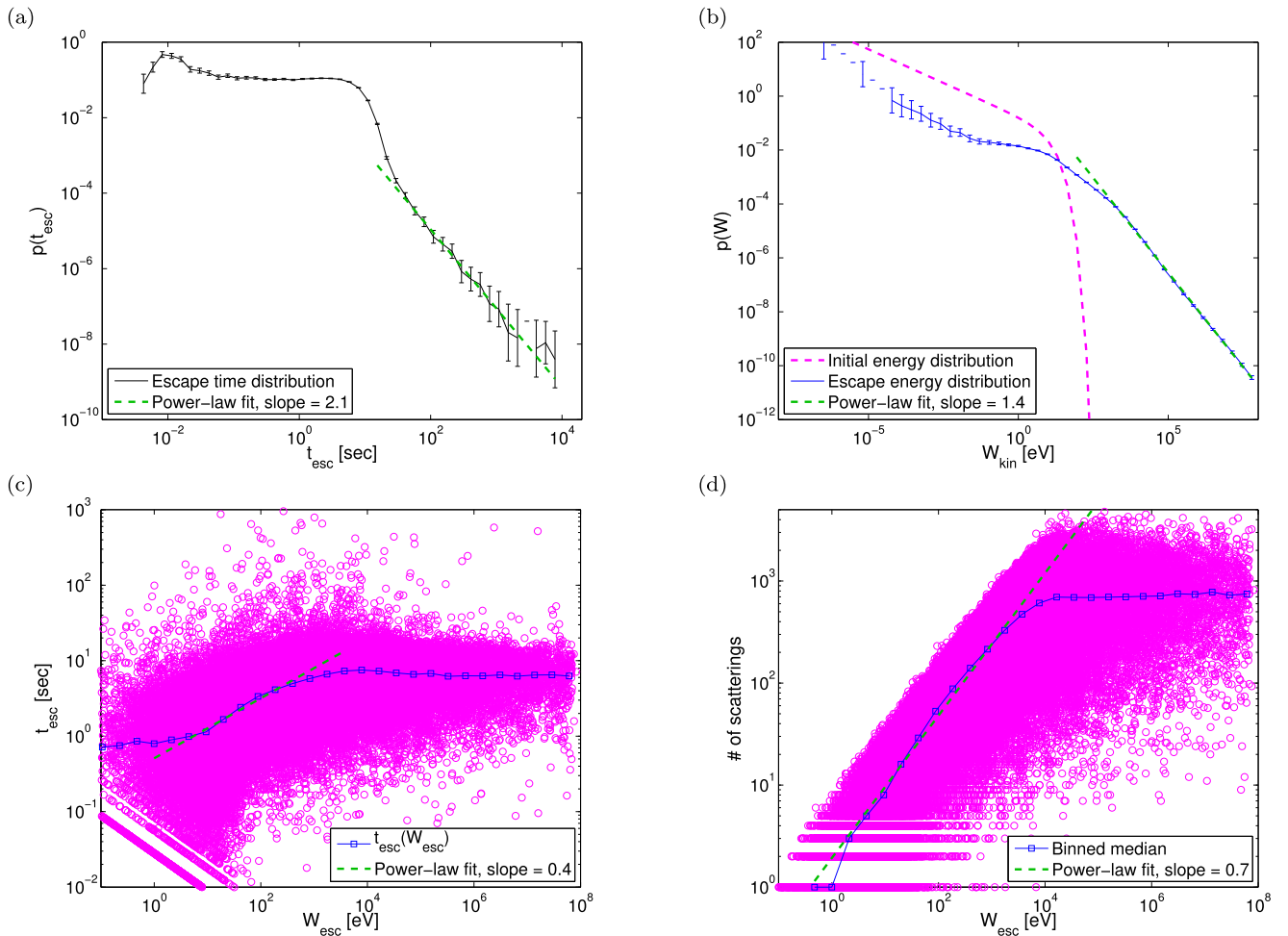
(a)

(b)

(c)

(d)

Figure 3. (a) Distribution of the escape times of the electrons. (b) Energy distribution of the electrons when they escape from the box. (c) Escape time as a function of the escape energy of the electrons. (d) Number of scatterings per particle as a function of the escape energy.
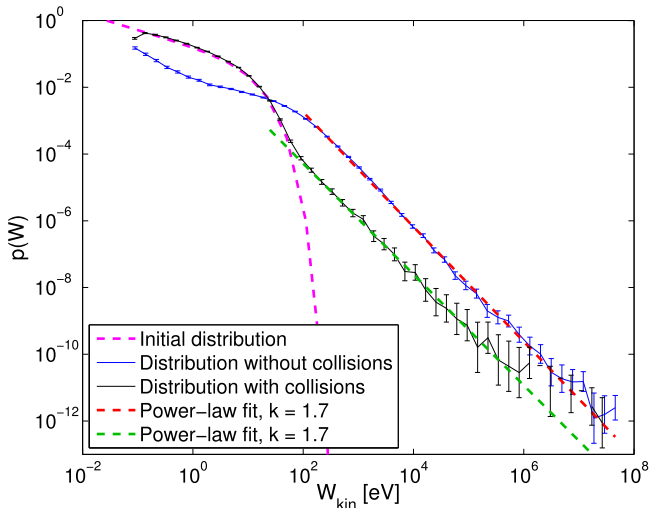

Figure 4. Energy distribution for electrons remaining inside the simulation box at $t = 0$ (magenta) and at $t = 4.5$ s with (black) and without (blue) collisions.
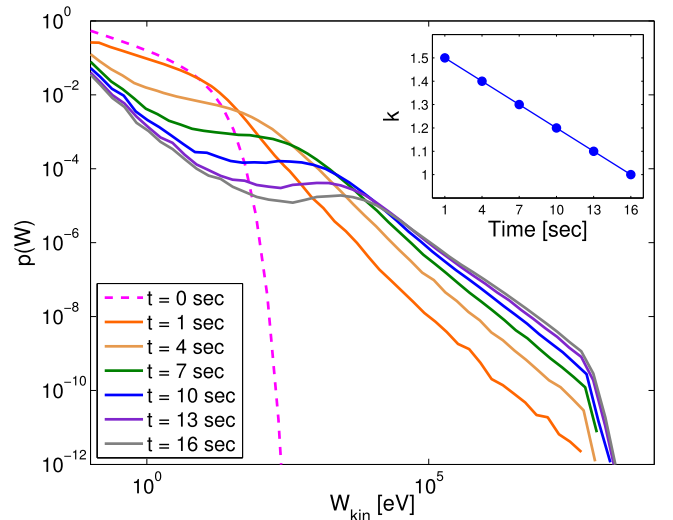
Figure 5. Evolution of the energy distribution until it reaches the asymptotic index $k = 1$. Inset: the evolution of the power-law index.

transport coefficients into the FP equation, Equation (6) (including the escape term, and with $Q = 0$), and solve the latter numerically, as described in Section 3.1, which, as shown in Vlahos et al. (2016), either can be successful in reproducing

the energy distribution of the test particles, or, as shown in Isliker et al. (2017), can fail to do so. In this case, through an analysis of the energy increments (Equation (15)), it can become obvious that only an FTE approach is appropriate. In
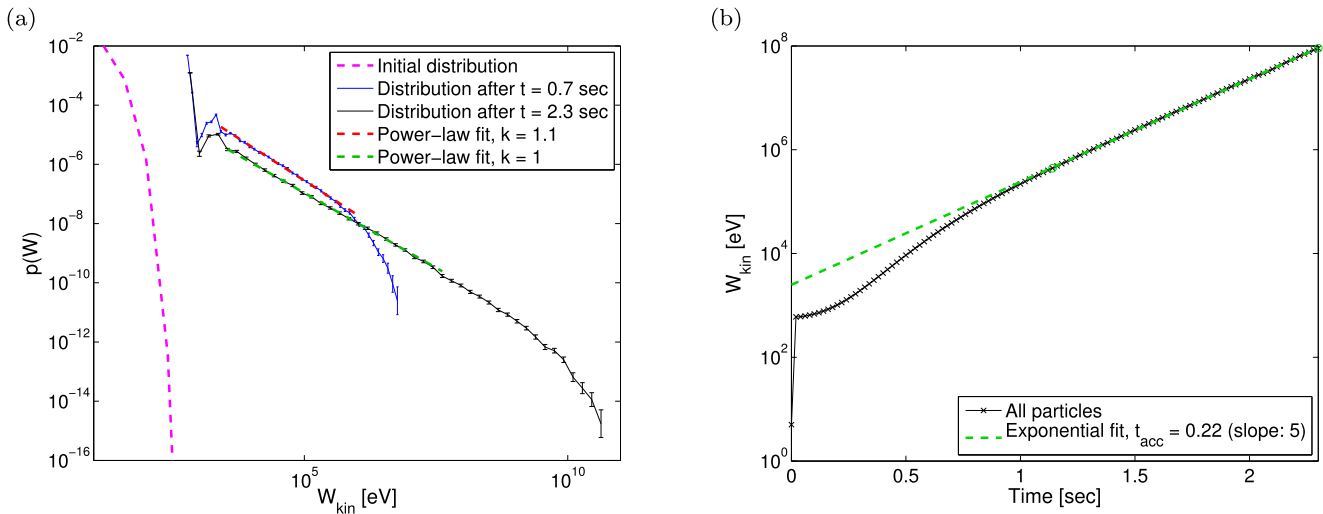
(a)

(b)

Figure 6. (a) Energy distribution at $t = 0$ s (magenta), $t = 0.7$ s (blue), and $t = t_{1/2} = 2.3$ s (black) for the electrons, together with the corresponding power-law fits, $k = 1.1$ (red) and $k = 1$ (green). (b) Mean kinetic energy of the electrons as a function of time (black) with an exponential fit (green).

the case of failure of the FPE, we determine the parameters of the FTE, Equation (16), and solve it numerically, in the way described in Section 3.2.

5.1. Electric Field Acceleration

5.1.1. Fokker–Planck Approach

We first consider acceleration by the electric field, and more specifically the case presented in Figure 2(a), for final time 1 s, with open boundaries, and without collisions. In Figure 7(a), the diffusion and convection coefficients at $t = 1$ s, as functions of the energy, are presented. There is a high level of noise in the estimate, which is a first indication that the FP approach might be problematic. Although there is no obvious functional form in the data, we performed a power-law fit to them in the higher-energy part above 1 keV, which yields the power-law indexes $a_D = 0$ and $a_F = 0.59$. For energies below 1 keV, we interpret the data as the two transport coefficients being constant. In order to verify the estimates of the transport coefficients, we insert them in the form of the fit into the FP equation (Equation (6)) and solve the FP equation numerically. The resulting energy distribution is shown in Figure 7(b), together with the energy distribution from the lattice gas model. There is obviously a large discrepancy between the FP solution and the particles' energy distribution—the FP solution is basically flat in the entire energy range, whereas the particles' distribution shows a decaying and extended power-law tail.

One might attribute the failure of the FP approach to the choice of fit we made to the transport coefficient data in Figure 7(a) and try to improve it. Yet, there is an inherent problem in the estimate of the transport coefficients that becomes obvious when considering the distribution of energy increments $p(w)$ that we show in Figure 7(c). This distribution exhibits an extended power-law shape, with index -1.56. From the definition of the energy increments in Equation (15), it is clear that the transport coefficients $F(W)$ and $D(W)$ (Equations (4) and (5)) are basically the first and second moments of the distribution of the energy increments, and thus they theoretically are infinite. In practice, when estimated with binned statistics, they are dominated by statistical noise. In other words, in the case at hand, the concept of transport coefficients in the classical sense is ill-defined.

5.1.2. FTE Approach

Given that the distribution of energy increments $p(w)$ has a power-law tail like the stable Levy distributions, we proceed to the FTE as a transport model to reproduce the particles' energy distribution. The order of the fractional derivative α can be inferred from the index z of the power-law tail of $p_w(w)$ in Figure 7(c) as $\alpha = -z - 1 = 0.56$. On the other hand, the characteristic function method (see Section 3.2 and Equation (14)) yields $\alpha = 0.66$ and $a = 0.066$ for the scale parameter. Figure 7(e) shows the numerical solution of the FTE at time $t = 1$ s, using α as estimated through the characteristic function method, together with the particles' energy distribution. The FTE successfully reproduces the power-law tail of the particles' distribution in its entire extent.

When changing the scale parameter a, we find that it does not affect the shape and power-law index of the FTE's solution; it just causes a shift of the solution in the vertical direction. We also find that the characteristic function method is not very precise in its estimate of the scale parameter a, so that we rather consider the estimate of a as indicative and change it to fine-tune the coincidence of the FTE solution with the particle data in the vertical direction of the plot. For Figure 7(e), we finally used a value of $a = 3.33$. After all, with the methods employed, we achieve a reasonable precision in the estimate of the order of the fractional derivative, and we get indicative values for the scale parameter; obviously, though, quantitatively more precise methods are desired and should be investigated, above all for the latter.

5.2. Acceleration at Contracting Islands

5.2.1. Fokker–Planck Approach

We now turn to acceleration at contracting islands, considering the case presented in Figure 6(a), for the final time 0.7 s, with open boundaries, and without collisions. Figure 8(a) presents the diffusion and convection coefficients at $t = 0.7$ s, as functions of energy. There now is a clear functional form of the data, both transport coefficients are of power-law shape, and a power-law fit in the higher-energy part above 5 keV yields the power-law indexes $a_D = 1.62$ and $a_F = 0.90$. For energies below 5 keV, the two transport coefficients turn over and vanish. We again insert them in the form of the fit into the FP equation, Equation (6), and
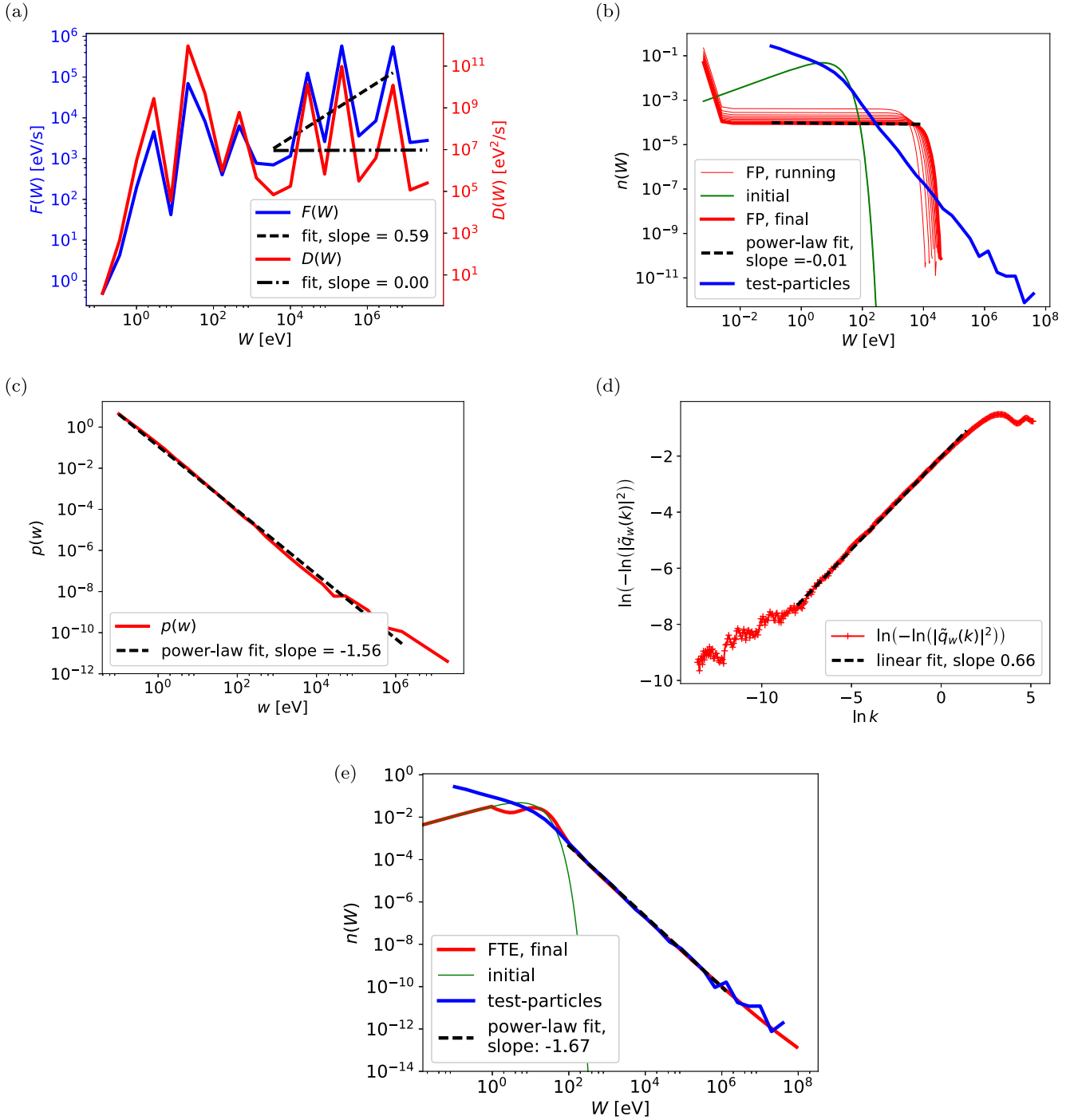
Figure 7. Acceleration by electric fields. (a) Convective F and diffusive D transport coefficients as a function of W at $t = 1$ s. (b) Solution of the FP equation, together with the energy distribution from the lattice gas simulation. (c) Distribution $p(w)$ of energy increments w. (d) Estimator of the characteristic function. (e) Solution of the FTE, together with the energy distribution from the lattice gas simulation.

solve the latter numerically. Figure 8(b) shows the resulting energy distribution together with the energy distribution from the lattice gas model. There is again a large discrepancy between the FP solution and the particles' energy distribution; the FP solution here is of extended power-law shape, yet with a slope clearly different from the one of the particles' distribution.

In contrast to the electric field acceleration, the estimate of the transport coefficients and the fit to them in Figure 8(a) do not show obvious signs that the FP approach might fail. The distribution of energy increments is shown in Figure 8(c); it is roughly of the same large extent as in the case of electric

field acceleration, it exhibits a power-law part between 5 and 50 keV, with index -1.1, and there is a turnover toward the highest energies. The large extent of the distribution and the partial power-law scaling indicate that also here the acceleration process is closer in nature to a random walk with Lévy flights than to classical Brownian motion.

5.2.2. FTE Approach

We thus turn to the question whether the FTE is also appropriate as a transport model in the case of acceleration at
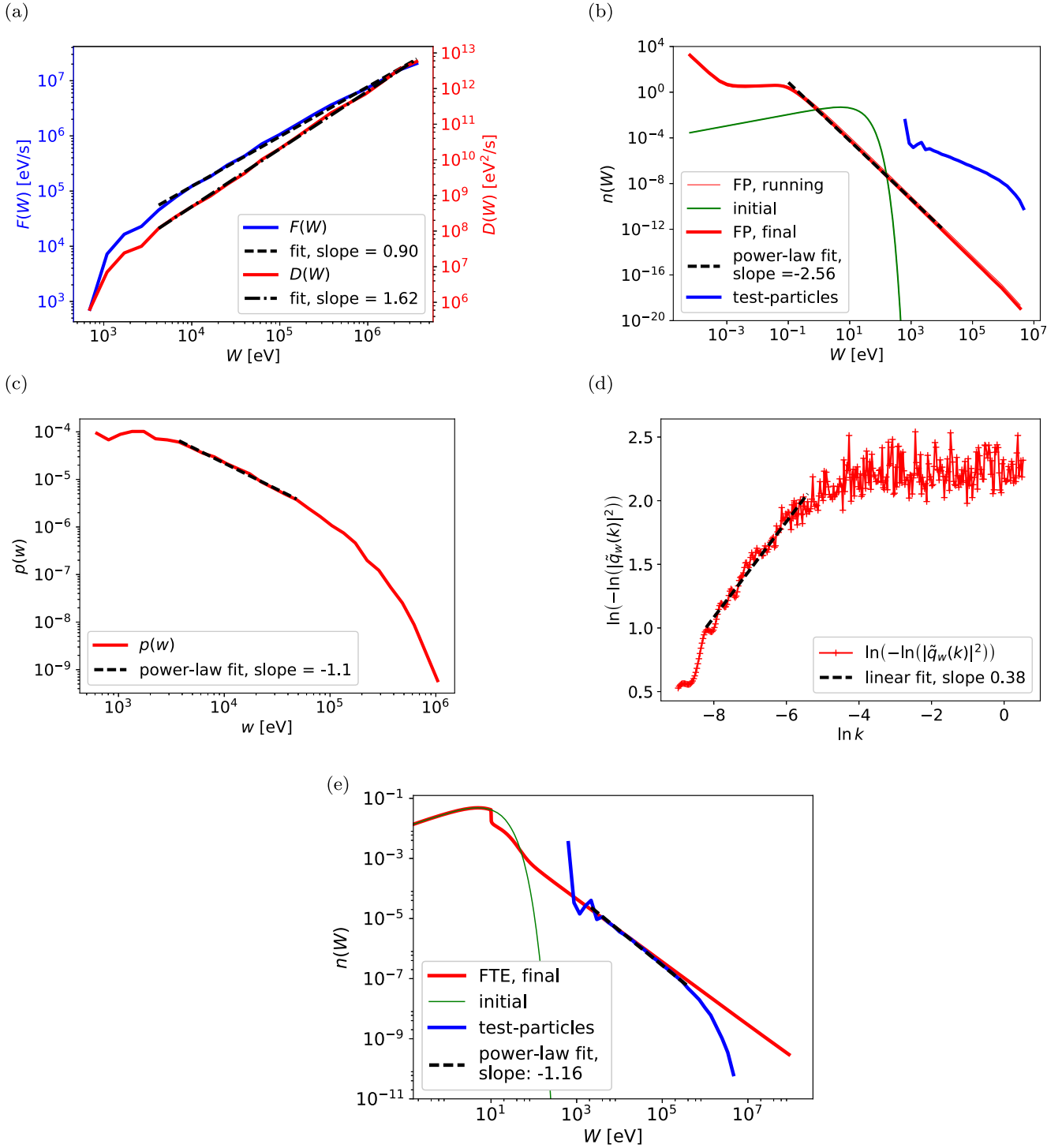
Figure 8. Acceleration at contracting islands. (a) Convective F and diffusive D transport coefficients. (b) Solution of the FP equation, together with the energy distribution from the lattice gas simulation. (c) Distribution $p(w)$ of the energy increments w. (d) Estimator of the characteristic function. (e) Solution of the FTE, together with the energy distribution from the lattice gas simulation.

contracting islands. The order of the fractional derivative α can be determined either from the index z of the power-law tail of $p_w(w)$ in Figure 8(c), which yields $\alpha = -z - 1 = 0.1$, or with the characteristic function method (see Section 3.2 and Equation (14)), which yields $\alpha = 0.38$ and $a = 29.8$ for the scale parameter. The characteristic function method is known in the literature not to be very precise for low values of α (i.e., close to 1; see, e.g., Borak et al. 2005), so that we will use here

the value of $\alpha = 0.1$ as inferred from the index z of the power-law tail of the increment distribution, and as before, we will consider the value of a to just be indicative.

Figure 8(e) shows the numerical solution of the FTE at time $t = 0.7$ s, together with the particles' energy distribution. The FTE here also successfully reproduces the power-law part of the particles' distribution (for the figure, we used a value of $a = 1.66$).

6. Summary and Discussion

It is well-documented in the current literature that the well-known nonlinear MHD structures, i.e., UCSs, strong turbulence, and shocks, will ultimately drive a turbulent reconnection environment. In this article, we analyzed the systematic acceleration of particles in a large-scale turbulent reconnection environment, either by the electric fields associated with the reconnection sites or by reflection at contracting islands. We showed that the energy distribution of the particles is always a power law above a certain energy. The power-law index depends on the characteristics of the interaction of the UCS with the particles, e.g., through the index of the power-law-distributed fluctuating magnetic field δB,; on the global properties of the magnetic topology, e.g., through the parameter λ_{sc}; and on the possible trapping of the particles, which will increase the escape time from the acceleration volume. For the electric field acceleration in the open simulation box, the power-law index is 1.7, and for the electric field acceleration with periodic boundary conditions (trapped particles), or acceleration by reflection at contracting islands, the power-law index asymptotically reaches the value of 1. Varying the initial temperature of the particles in the range from 10 to 100 eV does not affect the extent or the index of the power law formed. Both acceleration processes are extremely fast (of the order of milliseconds for the solar corona), the released energy is mainly absorbed by the energetic tail (the heating of the bulk distribution is not important), and collisions play only a minor role at low energies. For the open simulation box, the escape time for the low-energy particles increases with the escape energy, and it reaches a plateau for the high-energy particles. The acceleration time and the escape time are related to the mean free path in between the scatterings of the particles off the UCSs. For the particles accelerated by the electric fields in an open simulation box, the statistical properties of the UCSs (see Zhdankin et al. 2013) play a crucial role and determine the value of the power-law index of the energy distribution.

Our most important finding is that the applicability of the classical FP equation breaks down. This is manifested in the inability of the FP equation to reproduce the test particles' energy distribution, and in the practical difficulties of the expressions for F and D in Equations (4) and (3) to yield meaningful transport coefficients. The reason is that the transport in energy space is highly anomalous ("strange"); the particles move in energy space with increments that follow a power-law distribution, i.e., they perform Levy flights. We showed that in such cases of anomalous transport, an FTE, as introduced in Isliker et al. (2017), is appropriate, and it is indeed successful in reproducing the observed power-law distributions in energy.

The statistical analysis of the simulation data, in particular of the distribution of increments, allows one to decide whether a classical FP equation or an FTE is appropriate. In the case of normal transport, the estimate of the classical transport coefficients is based on the data. In the case of anomalous transport, there are several possibilities to statistically analyze the data. In principle, a stable Levy distribution could be fitted to the distribution of increments in order to determine the parameters of the FTE, which would have to be done in Fourier space, since the stable Levy distributions are known in analytical form only in Fourier space. The order of the fractional derivative is also directly given by the index of the power-law tail of the energy increments, and thus it is

straightforward to estimate. For the other parameters, such as the scale parameter a, we used the characteristic function method, which is not very accurate, and a better method is needed. After all, the form of the FTE and its parameters, most prominently the order of the fractional derivative, are directly inferred from the simulation data. We also note that the kind of data needed for this analysis can also be made available from PIC simulations and from test particles that are tracked in the fields of MHD simulations (as in Isliker et al. 2017).

In using the FTE, we made two simplifying assumptions: we considered only symmetric and one-sided distributions of increments, and for the time stepping (waiting times), we considered a fixed, small time interval, as it corresponds to the sampling of the particle evolution that we applied, and which leads to an ordinary derivative in the time direction. These assumptions did obviously not affect the success of the FTE approach we presented here. We also note that, from its derivation, the FTE is a tool to model the high-energy part (tail) of the distribution; the modeling of the low-energy part could possibly be achieved by combining the fractional term in the FTE with classical diffusive and convective terms, which we will address in a future work. Moreover, spatial transport could play an important role in the acceleration process—see, e.g., Bian et al. (2017)—and Figures 3(c) and (d) also give some indication that the spatial diffusion is of a rather complex nature.

Turbulent reconnection is a very efficient acceleration mechanism, yet it is not relevant for the heating of the ambient plasma. In most astrophysical sources, where particle acceleration is observed, the plasma is also heated impulsively. In a recent review on turbulent reconnection, Karimabadi et al. (2013) pointed out that "intermittent plasma turbulence will in general consist of both coherent structures and waves." They claim that the excitation of waves (or large-scale density fluctuations) is due to the motion of coherent structures. We propose that the combination of UCSs with the large-scale magnetic and density fluctuations that are generated by the motion of the UCSs can heat the plasma through stochastic Fermi energization (see Kontar et al. 2017; Pisokas et al. 2017) and it can efficiently accelerate the particles through the systematic Fermi acceleration discussed in this article.

ORCID iDs

Heinz Isliker ⓘ https://orcid.org/0000-0001-9782-2294
Loukas Vlahos ⓘ https://orcid.org/0000-0002-8700-4172

References

Achterberg, A. 1981, A&A, 97, 259
Achterberg, A. 1990, A&A, 231, 251
Ambrosiano, J., Matthaeus, W. H., Goldstein, M. L., & Plante, D. 1988, JGRA, 93, 14383
Anastasiadis, A., & Vlahos, L. 1991, A&A, 245, 271
Anastasiadis, A., & Vlahos, L. 1994, ApJ, 428, 819
Arzner, K., Knaepen, B., Carati, D., Denewet, N., & Vlahos, L. 2006, ApJ, 637, 322
Arzner, K., & Vlahos, L. 2004, ApJL, 605, L69
Bian, N. H., & Browning, P. K. 2008, ApJL, 687, L111

Bian, N. H., Emslie, A. G., & Kontar, E. P. 2017, ApJ, 835, 262
Biskamp, D., & Welter, H. 1989, PhFlB, 1, 1964
Borak, S., Härdle, W., & Weron, R. 2005, in Statistical Tools for Finance and Insurance, ed. P. Cizek, W. K. Härdle, & R. Weron (Berlin: Springer) 21–44
Boyd, J. P. 2001, Chebyshev and Fourier Spectral Methods (2nd edn.; New York: Dover Publications)
Burgess, D., Gingell, P. W., & Matteini, L. 2016, ApJ, 822, 38
Caprioli, D., & Spitkovsky, A. 2014a, ApJ, 783, 91
Caprioli, D., & Spitkovsky, A. 2014b, ApJ, 794, 46
Caprioli, D., & Spitkovsky, A. 2014c, ApJ, 794, 47
Cargill, P., Vlahos, L., Baumann, G., Drake, J., & Nordlund, Å. 2012, SSRv, 173, 223
Dahlin, J. T., Drake, J. F., & Swisdak, M. 2015, PhPl, 22, 100704
de Gouveia dal Pino, E. M., & Lazarian, A. 2005, A&A, 441, 845
Decker, R. B. 1988, SSRv, 48, 195
Dmitruk, P., Matthaeus, W., Seenu, N., & Brown, M. R. 2003, ApJL, 597, L81
Dmitruk, P., Matthaeus, W. H., & Seenu, N. 2004, ApJ, 617, 667
Drake, J. F., Opher, M., Swisdak, M., & Chamoun, J. N. 2010, ApJ, 709, 963
Drake, J. F., Swisdak, M., Che, H., & Shay, M. A. 2006, Natur, 443, 553
Drake, J. F., Swisdak, M., & Fermo, R. 2013, ApJL, 763, L5
Drury, L. O. 1983, RPPh, 46, 973
Fermi, E. 1949, PhRv, 75, 1169
Fermi, E. 1954, ApJ, 119, 1
Galsgaard, K., & Nordlund, Å. 1996, JGR, 101, 13445
Gardiner, C. 2009, Stochastic Methods: A Handbook for the Natural and Social Sciences (Berlin: Springer)
Gillespie, D. T. 1996, PhRvE, 54, 2084
Gordovskyy, M., & Browning, P. K. 2011, ApJ, 729, 101
Guo, F., Li, H., Daughton, W., & Liu, Y.-H. 2014, PhRvL, 113, 155005
Guo, F., Liu, Y.-H., Daughton, W., & Li, H. 2015, ApJ, 806, 167
Hoshino, M. 2012, PhRvL, 108, 135003
Hoshino, M., & Lyubarsky, Y. 2012, SSRv, 173, 521
Hughes, B. D. 1995, Random Walks and Random Environments, Vol. 1: Random Walks (Oxford: Clarendon Press)
Isliker, H., Vlahos, L., & Constantinescu, D. 2017, PhRvL, 119, 045101
Karimabadi, H., & Lazarian, A. 2013, PhPl, 20, 112102
Karimabadi, H., Roytershteyn, V., Daughton, W., & Liu, Y.-H. 2013, SSRv, 178, 307
Karimabadi, H., Roytershteyn, V., Vu, H. X., et al. 2014, PhPl, 21, 062308
Karimabadi, H., Roytershteyn, V., Wan, M., et al. 2013, PhPl, 20, 012303
Kilbas, A. A., Srivastava, H. M., & Trujillo, J. J. 2006, Theory and Applications of Fractional Differential Equations (Amsterdam: Elsevier)
Kirk, J. G., & Dendy, R. O. 2001, JPhG, 27, 1589
Klafter, J., Blumen, A., & Shlesinger, M. F. 1987, PhRvA, 35, 3081
Klages, R., Radons, G., & Sokolov, I. M. 2008, Anomalous Transport: Foundations and Applications (Weinheim: Wiley-VCH)

Kontar, E., Perez, J., Harra, L., et al. 2017, PhRvL, 118, 155101
Koutrouvelis, I. A. 1980, J. Am. Stat. Assoc., 75, 918
Kowal, G., de Gouveia Dal Pino, E. M., & Lazarian, A. 2011, ApJ, 735, 102
Krymskii, G. F. 1977, DoSSR, 234, 1306
Kulsrud, R. M., & Ferrari, A. 1971, Ap&SS, 12, 302
Lazarian, A., & Opher, M. 2009, ApJ, 703, 8
Lazarian, A., Vlahos, L., Kowal, G., et al. 2012, SSRv, 173, 557
Lee, M. A., Mewaldt, R. A., & Giacalone, J. 2012, SSRv, 173, 247
Lenard, A., & Bernstein, I. B. 1958, PhRv, 112, 1456
Longair, M. S. 2011, High Energy Astrophysics (Cambridge: Cambridge Univ. Press)
Matsumoto, Y., Amano, T., Kato, T. N., & Hoshino, M. 2015, Sci, 347, 974
Matthaeus, W. H., Ambrosiano, J. J., & Goldstein, M. L. 1984, PhRvL, 53, 1449
Matthaeus, W. H., & Lamkin, S. L. 1986, PhFl, 29, 2513
Matthaeus, W. H., & Montgomery, D. 1980, NYASA, 357, 203
Matthaeus, W. H., & Velli, M. 2011, SSRv, 160, 145
Melrose, D. B. 1994, ApJS, 90, 623
Miller, J. A., Cargill, P. J., Emslie, A. G., et al. 1997, JGR, 102, 14631
Miller, J. A., Guessoum, N., & Ramaty, R. 1990, ApJ, 361, 701
Montroll, E. W., & Weiss, G. H. 1965, JMP, 6, 167
Onofri, M., Isliker, H., & Vlahos, L. 2006, PhRvL, 96, 151102
Petrosian, V. 2012, SSRv, 173, 535
Pisokas, T., Vlahos, L., Isliker, H., Tsiolis, V., & Anastasiadis, A. 2017, ApJ, 835, 214
Podlubny, I., Chechkin, A., Skovranek, T., Chen, Y., & Vinagre Jara, B. M. 2009, JCoPh, 228, 3137
Podlubny, I., Skovranek, T., Vinagre Jara, B. M., et al. 2013, RSPTA, 371, 20120153
Priest, E. 2014, Magnetohydrodynamics of the Sun (Cambridge: Cambridge Univ. Press)
Ragwitz, M., & Kantz, H. 2001, PhRvL, 87, 254501
Schneider, P. 1993, A&A, 278, 315
Schure, K. M., Bell, A. R., O'C Drury, L., & Bykov, A. M. 2012, SSRv, 173, 491
Servidio, S., Dmitruk, P., Greco, A., et al. 2011, NPGeo, 18, 675
Turkmani, R., Vlahos, L., Galsgaard, K., Cargill, P., & Isliker, H. 2005, ApJL, 620, L59
Uritsky, V. M., Pouquet, A., Rosenberg, D., Mininni, P. D., & Donovan, E. F. 2010, PhRvE, 82, 056326
Vlahos, L., Isliker, H., & Lepreti, F. 2004, ApJ, 608, 540
Vlahos, L., Pisokas, T., Isliker, H., Tsiolis, V., & Anastasiadis, A. 2016, ApJL, 827, L3
Zank, G. P., Hunana, P., Mostafavi, P., et al. 2015, ApJ, 814, 137
Zhdankin, V., Uzdensky, D. A., Perez, J. C., & Boldyrev, S. 2013, ApJ, 771, 124